CURVATURE EFFECTS IN THE CURVED DUCT FOR THE COMPRESSIBLE VISCOUS FLOW

Kougen OZAKI*, Hiroshi MAEKAWA**
***Hiroshima University, **Hiroshima University**

Keywords: *compressible flow, curvature effects, transition*

Abstract

In this paper, non-reflecting boundary conditions based on characteristic boundary conditions for the three dimensional compressible Navier-Stokes equations (here after referred as NSCBC), especially outflow boundary conditions, are examined and numerical tests for a curved duct flow are made. Using the subsonic non-reflecting outflow boundary conditions, curvature effects in the curved duct for the compressible flow in a transonic range are investigated. Extensive numerical tests of the stability of the numerical solution and the efficiency of the subsonic non-reflecting outflow boundary conditions extended to three-dimensional problems show that the NSCBC method provides accurate results for very low Reynolds number flows with isothermal no-slip walls. The unsteady Navier-Stokes equations in terms of cylindrical coordinates were numerically solved using high-order compact schemes. For the high curved ducts flows with Re=400.0 and Mc=0.4, using different wall boundary conditions of with/without heat transfer, preliminary results were presented. For the density profiles at the cross section, the density gradient in the z-direction is flatter than that in the radial direction in both cases due to the curved duct effects. Finally, using the same boundary conditions and the high-order compact schemes, three cases of Dean numbers up to 442 with Re=700 and Mach=0.7 were investigated to understand the curvature effects for the compressible viscous flows. To understand the essential stream-wise structure, helicity structures are presented in this paper. Due to the induced velocity by the strong interaction between a pair of stream-wise vortices in the curved duct, the helical structure of the helicity is observed around the 60-degrees section where the secondary flow develops into a 4-cell state. The generalized inflection points appear for the steady flow largely due to the stream-wise velocity distribution. Near the top/bottom and concave walls, the gradient of stream-wise velocity at the inflection point is steep with a maximum shear, which will lead to substantial transition to turbulence in the curved duct flows.

1 Introduction

In recent years, the technology of turbo machinery in small size, such as micro gas turbines for distributed power generation, are paid much attention. It is a time when developments within micro turbine technology are moving fast as lightening. Technical insight will bring us an invaluable analysis of technical work ongoing at micro turbine developments. Since the micro turbine rotates at high speed; for example, at the maximum rotation speed 96,000 *rpm*, the gas flow inside the turbine reaches a sonic range. Therefore, to develop more reliable and high efficiency micro turbines, it is too indispensable to solve flows through a narrow inlet at a high speed. This means that an analysis requires viscous and compressible flows. Long curved duct flows with a small gap are important to analyze the viscous flow between turbine blades. For such the small size turbine, *Reynolds* number of the flow tends to be lower as much as we can treat in *DNS* (*Direct Numerical Simulation*).

For *DNS*, the *NSCBC* [1] strategy by *Poinsot and Lele* supplies useful boundary conditions to solve simple flows such as plane flows with low *Reynolds* and low *Mach* numbers between parallel walls: *the Poiseuille* flow. They investigated only *2D* problems. For *3D* problems, flows are more complex than that in *2D* because of various influences, i.e. curvature effect, which are significant for fluid problems where flow reaches near sonic range by using the *NSCBC* because of the theoretical difficulties. For practical problems, flows have high *Reynolds* and *Mach* numbers. Among significant problems in curved systems, essential features such as roles of secondary flows affected by compressibility, heat convection and so on haven't been analyzed yet. Therefore, flows with heat transfer from the curved duct walls were simulated to study curvature effects, including viscous, compressible and heat transfer effects in flows.

2 Numerical methods

2.1 Governing equations

The compressible governing equations are reviewed below. Note that in the set of the *Navier-Stokes equations* (here after referred as *N-S equations*), all distances are normalized by the half duct width *a/2* and all velocities by sonic speed at the wall.

$$\frac{\partial \rho}{\partial t}+\frac{1}{r}\frac{\partial}{\partial r}(r\rho u_r)+\frac{1}{r}\frac{\partial}{\partial \theta}(\rho u_\theta)+\frac{\partial}{\partial z}(\rho u_z)=0, \quad (1)$$

$$\frac{\partial e}{\partial t}+\frac{1}{r}\frac{\partial}{\partial r}\{r(e+p)u_r\}+\frac{1}{r}\frac{\partial}{\partial \theta}\{(e+p)u_\theta\} \quad (2)$$
$$+\frac{\partial}{\partial z}\{(e+p)u_z\}=\frac{1}{Re}Terms(e)$$

$$\frac{\partial}{\partial t}(\rho u_r)+\frac{\partial}{\partial r}(\rho u_r^2)+\frac{1}{r}\frac{\partial}{\partial \theta}(\rho u_r u_\theta)+\frac{\partial}{\partial z}(\rho u_r u_z), \quad (3)$$
$$+\frac{\rho}{r}(u_r^2-u_\theta^2)+\frac{\partial p}{\partial r}=\frac{1}{Re}Viscous\,Terms(u_r)$$

$$\frac{\partial}{\partial t}(\rho u_\theta)+\frac{\partial}{\partial r}(\rho u_r u_\theta)+\frac{1}{r}\frac{\partial}{\partial \theta}(\rho u_\theta^2)+\frac{\partial}{\partial z}(\rho u_\theta u_z), \quad (4)$$
$$+2\frac{\rho u_r u_\theta}{r}+\frac{1}{r}\frac{\partial p}{\partial \theta}=\frac{1}{Re}Viscous\,Terms(u_\theta)$$

$$\frac{\partial}{\partial t}(\rho u_z)+\frac{\partial}{\partial r}(\rho u_r u_z)+\frac{1}{r}\frac{\partial}{\partial \theta}(\rho u_\theta u_z)+\frac{\partial}{\partial z}(\rho u_z^2) \quad (5)$$
$$+\frac{\rho u_r u_z}{r}+\frac{\partial p}{\partial z}=\frac{1}{Re}Viscous\,Terms(u_z).$$

Eqs.(1), (2) and (3)-(5) represent for mass, total-energy and momentum conservation laws, respectively. Dissipation term for total energy; *Eq.*(2) involves heat flux as shown in *Eq.*(6).

$$Terms(e)=\frac{1}{(\gamma-1)Pr}div(\mu\,grad\,T)+\vec{\tau}:grad\,\vec{U}, \quad (6)$$

wher the total energy *e* is defined as

$$e=\frac{1}{2}\rho\left|\vec{U}\right|^2+\frac{p}{\gamma-1}. \quad (7)$$

For closure problem, the following equations are introduced; the perfect gas state equation and a power law for dynamic viscosity.

$$T=\gamma\frac{p}{\rho}, \quad (8)$$

$$\mu=T^{2/3}, \quad (9)$$

where (=1.4) is the specific heat and *Pr* (=0.72) is the *Prandtle number* of typical compressible gas condition for air.

2.2 Numerical schemes

To obtain spatially accurate numerical solutions to the governing equations, high-order (sixth-order) *compact schemes* [2] are employed. The compact approximations for the first and second derivatives are expressed in the following linear combinations:

$$\frac{1}{3}f'_{i-1}+f'_i+\frac{1}{3}f'_{i+1}=\frac{1}{9}\frac{f_{i-2}-f_{i+2}}{4h}+\frac{14}{9}\frac{f_{i-1}-f_{i+1}}{2h},$$

$$\frac{2}{11}f''_{i-1}+f''_i+\frac{2}{11}f''_{i+1}$$
$$=\frac{3}{11}\frac{f_{i-2}-2f_i-f_{i+2}}{4h^2}+\frac{12}{11}\frac{f_{i-1}-2f_i-f_{i+1}}{h^2}$$

where $f_i'\equiv\frac{\partial}{\partial x_i}f(x_i)$ and $f_i''\equiv\frac{\partial^2}{\partial x_i^2}f(x_i)$ at node *i*.

Here, we consider a uniform spaced mesh where the nodes are indexed by *i*. The third-order derivatives at the boundary *i*=0 are given by

$$f'_0+2f'_1=\frac{1}{h}\left(-\frac{5}{2}f_0+2f_1+\frac{1}{2}f_2\right),$$

$$f''_0+11f''_1=\frac{1}{h^2}(13f_0-27f_1+15f_2-f_3).$$

The derivatives and their expressions at the boundaries are written in the following matrix formulations:

$$B_1 \hat{f}' = \frac{1}{h} C_1 \hat{f},$$

$$B_2 \hat{f}'' = \frac{1}{h^2} C_2 \hat{f}$$

where **B** and **C** are $N \times N$ sparse matrices, and $\hat{f}$, $\hat{f}'$ and $\hat{f}''$ are N vectors representing the values of the function and its derivative at the nodes, respectively. An explicit *Euler* method with second order accuracy is employed for time advancement. The time step is 0.001 for a $81 \times 81 \times 41$ ($r \times \theta \times z$) compuational grid.

2.3 NSCBC; boundary conditions

An available method for the viscous compressible flows, *NSCBC* [1], is employed in this study. Note that handling of outflow boundary has serious problems yet in this method when the flow is near transonic state. This problem has been corrected by numerical experiments for a flow of very low *Reynolds* and very low *Mach* numbers. An estimation of the wave amplitude L_1 coming from the outer regions of the simulation domain is given mathematically as

$$L_1 = (u_i - c) \left(\frac{\partial p}{\partial x_i} - \rho c \frac{\partial u_i}{\partial x_i} \right). \qquad (10)$$

Instead of using the characteristic relation of Eq.(10), following empirical forms are employed for outflow boundary conditions.

$$L_1 = K(p - p_\infty), \qquad (11)$$

$$K = \sigma \left(1 - M^2 \right) \frac{c}{L}, \qquad (12)$$

where σ is constant value evaluating by numerical experiments, M is the maximum *Mach number* in the computational domain, L is the characteristic length of the computational domain such as channel length and the subscript of derivatives, i, is the flow direction. In the *NSCBC* report [1], numerical experimental value of =0.25 gives good agreements with an exact solution for *plane Poisuille flow* that satisfies following conditions;

$$\frac{L}{l} Re^{-1} M^2 \ll 1,$$

where Re =15.0, *Mach* =0.1 and L/l =10.0.

3 Numerical results and discussions

3.1 Preliminary tests for developed code
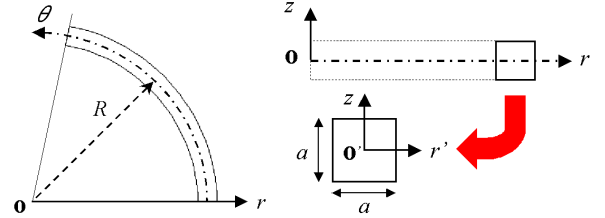
Skecth.1. Cylindrical coordinate for curved duct.

Case	Dn	Rc	R	a
0	200.0	3.5	7.0	2.0

Table.1. Parameters of the curved duct for bench mark test: R; central radius curvature of duct, a; duct width and R_c (= R/a); aspect ratio.

First, we briefly describe preliminary results done with different duct wall conditions: adiabatic or isothermal with no-slip walls. Skecth.1 shows the cylindrical coordinate system with symbols used in this study. Flow is chosen for D_n =200 defined as *Eq*.(13) with *Re* =400.0 and *Mach*=0.4.

$$D_n \equiv Re / R_c^{1/2}, \qquad (13)$$

The duct parameters using in this test are shown in Table.1. In this simulation, L/l =10.0 is employed for the outlet boundary conditions at θ =72.0 degrees. For the inflow conditions, the inlet stream-wise velocity u_θ is a parabolic profile for the r'-z plane, which is given a straight duct by incompressible experiments [6]. The inlet velocity and temperature is treated as steady state. These conditions are shown as follows.

$$\begin{cases} u_\theta(r,0,z,t) = u_\theta(r,0,z) \\ u_r(r,0,z,t) = u_z(r,0,z,t) = 0.0 \\ T(r,0,z,t) = 1.0 \end{cases}$$

There is no secondary flow at the inlet. This is an adequate approximation for very low *Re*.
At t = 200 steps when flows are fully developed, the pressure distributions along downstream wise distances at z=0.0 are shown in Fig.1, where red, black and blue lines indicate the pressure at the outside wall, the central position of the duct width at *r=R* and the inside wall,

respectively. As seen in incompressible case [3], a pressure peak at the outside wall appears for the each case. In the section at the pressure peak, distributions of the stream-wise velocity u_θ and the pressure are similar to each case. See Fig.2(a) for adiabatic case. Because of the very low *Re* and *Mach* numbers flow, there is no appreciable difference appears in the distributions of the stream-wise velocity u_θ and the pressure with different wall conditions. Profiles of the stream-wise velocity u_θ and the pressure in the outlet section at θ=72.0 degrees are similar to each other, as seen in Fig.2(b) for adiabatic case. Here, Fig.3(b) indicates the secondary flow obtained by the *NSCBC* method in the outlet section at θ=72.0 degrees. The secondary flow at the outlet is called as a *2-cell* state [6] that occurs in flows with very low *Re*. Note that the bottom figures in Fig.3 indicate the distributions of *helicity*, *H*, defined as the following form:

$$H \quad U \bullet \quad .$$

Obviously, from this definition, this quantity indicates the essential stream-wise structure involving three-dimensional vortices effect. Note that *helicity* depends on the coordinate systems because of the pseudo-scalar. It dose not appear for the systems where there is no inner product of velocity and vorticity such as time-averaged field of *the Poisuille flow*. Discussions about *helicity* are mentioned later. In both cases, the amplitude of secondary flow in Fig.3(a) reaches near 20% of the maximum typical stream-wise velocity at θ=29-degrees section where the magnitude of the secondary flow is the highest. Near the outlet section, the strength of the secondary flow around the top/bottom wall is higher than the other regions. For incompressible cases, this kind of structure is also observed in the reports [3,4,6,7]. In this case, the secondary flow at further downstream sections may be a *2-cell* state due to very low D_n flow.

Fig.4 shows the distributions of density and temperature for each case. For the adiabatic case, Fig.4(a) shows that high temperature flows caused by fluid friction on the walls gather around the inside wall due to the secondary flow.
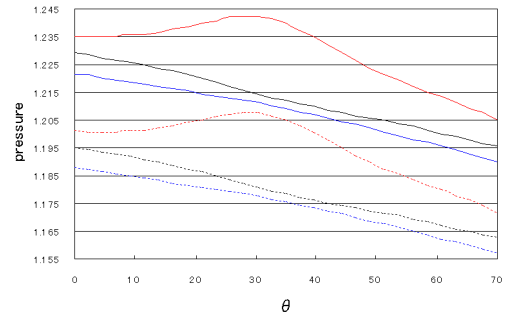

Fig.1. Pressure distribution along downstream-wise distance at *z*=0.0, red line: *r'*=1.0, black line: *r'*=0.0 and blue line: *r'*=-1.0 (solid: adiabatic, dotted: iso-thermal)
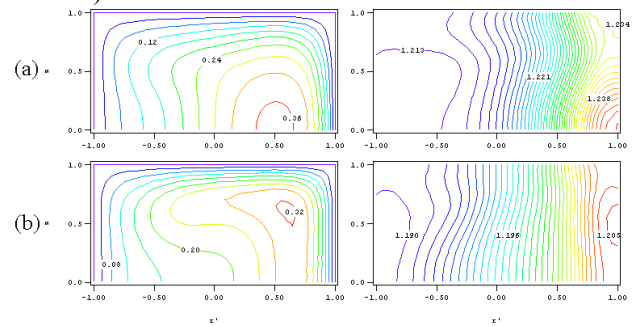

Fig.2 Contour lines of stream-wise velocity (left) and pressure (right) in the half-top section for adiabatic case at (a) θ=29-degrees and (b) outlet sections.

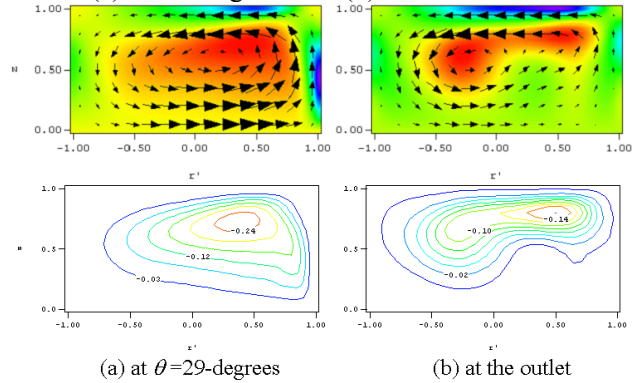(a) at θ=29-degrees   (b) at the outlet

Fig.3 Top; distributions of secondary flow (arrow) with ω_θ (red; negative and violet; positive) and bottom; contours of *helicity*.
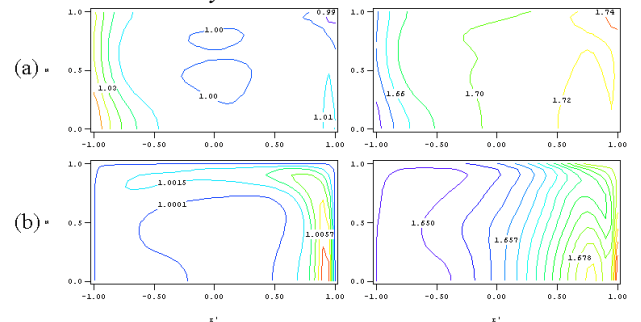

Fig.4 Contours of temperature (left) and density (right) at the θ=29-degrees sections for (a) adiabatic and (b) isothermal case.

On the contrary, for the isothermal case, Fig.4(b) shows that temperature T is kept about constant of T=1.0 in the section. By absorbing frictional heats on the walls, T is found to be about constant over the duct section. A comparison of the density distributions for both cases shows a remarkable difference around the top/bottom walls. Because the distribution of the pressure is the same in Fig.2(a), the change of density in the z-direction is found to be not due to the pressure gradients. This may be a significant phenomena associated with the appearance of inflection points as mentioned later.

3.2 Curvature effects for flows with isothermal walls

In order to study the curvature effect on evolution of the flow structure, *DNS*s for higher D_n with *Re*=700 and *Mach*=0.7 were performed. Note that the duct wall condition was chosen to be isothermal walls. The inflow conditions are the same as stated in the preliminary tests. Table.2 indicates the parameters of the curved ducts using this study and these shapes are shown in Fig.5. As seen in Fig.5, the outlet is at the θ=120-degrees for all cases. Note that the outflow boundary conditions for case.   have a numerical problem to be overcome as the 3-dimentional outflow boundary condition because the characteristic length of the inside wall is lower than L=10.0 as shown in Table.3. Then, we examined the use of L=10.0 with σ=0.25 for the outflow boundary conditions.

At t = 200, flows are fully developed and steady states are obtained. Fig.6 shows the development of secondary flow along the duct length for each case. As seen in Fig.6(c), a *4-cell state* [6,7] appears around at the θ = 90-degrees section for each case. Here, Fig.6(d) in case.   shows a quasi *6-cell state* [7] in the vorticity field at the outlet section. Fig.7 indicates the distribution of radial velocity u_r along with the duct length of θ at r' =0.8 and z =0.0, which is different from the incompressible case [7]. The magnitude of the secondary flow in case.   reaches about 14% of the inlet maximum velocity at the θ=90-degrees section,

Case	Dn	Rc	R	a
I	313.0	5.0	10.0	2.0
II	361.5	3.8	7.5	2.0
III	442.7	2.5	5.0	2.0

Table.2. Parameters of the curved ducts.

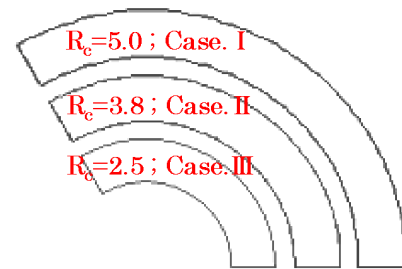|	R	Duct length		
		Center	Inside	Outside
case.I	10.0	20.9	18.8	23.0
case.II	7.5	15.7	13.6	17.8
case.III	5.0	10.5	8.4	12.6

Table.3. Comparison of duct length for each case.

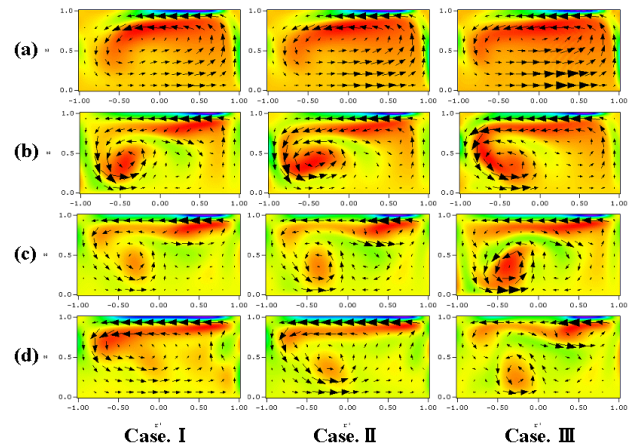Fig.5.Comparison of r-θ shape for each case.

Fig.6. Distribution of stream-wise vorticity ω_θ (red; negative and violet; positive) with secondary flow (arrow) for each duct case at θ = (a) 30, (b) 60, (c) 90 and (d) 120-degrees sections.
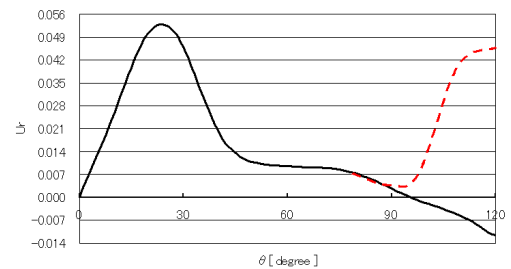

Fig.7. Distribution of radial velocity u_r based on sonic speed at the wall along azimuthal direction θ for case.   at r'=0.8 and z=0.0; solid line: *DNS* data in this study and dotted line: incompressible case with a *6-cell state* [7].

where a *4-cell* state appears. Increasing the D_n number to 442.7 increases the magnitude of the secondary flow, as shown in case.   , the magnitude in case.   is 1.5 times larger than that in case.   at the θ =90-degrees section.

As seen in Figs.6(b)-(d), a pair of vortices is moving to the origin of *r'-z* plane. Increasing the D_n number leads to the stronger induced velocity and the shorter distance between a pair of vortices, as illustrated in Skecth.2(a). At the outlet section, these vortices reaches around at the region of *r'* = -0.25 and *z* = 0.25, while the secondary flow develops different to each other. Fig.8 shows the development of *helicity* along the duct length of θ for case.   . Fig.9 shows the 3-dimentional structure of *helicity* in the half-bottom part of the duct for case.   . Skecth.2(b) indicates illustration of the 3-dimentional structure of *helicity*. It is interesting to note that as shown in Fig.9 the helix of *helicity* itself appears around at the θ = 45-degrees section where a *2-cell* state evolves into a *4-cell* state. Here after, this structure is referred to as H^2-structure. Appearance of the H^2-structure is explained as follows. The distance between a pair of vortices is so short that the stronger induced velocity is generated at the *z*=0.0 plane for high D_n flows. Figs.6(b)-(d) indicates generation of the induced velocity because the secondary flow at the *z*=0.0 plane between a pair of vortices is higher than that in other *r'* locations. During the process of vortices moving by the induced velocity, a pair of separated *helicity* structures meets at the central part of the section. Further more, because of the elliptical shape of the separated vortex shown in Figs.8(c)-(f), H^2-structure forms in the curved duct flow.

In this study, the *helicity* separated from a mass of *helicity* creeping along the top/bottom wall, which is weaken by the viscous effect in low *Re* flow. Therefore, if *Re* is much higher as practical case, this separated *helicity* structure should be maintained with its magnitude further downstream. On the contrary, very low *Re* flow doesn't have a structure of the separated *helicity* as shown in Fig.10 that is show in the preliminary case mentioned above.
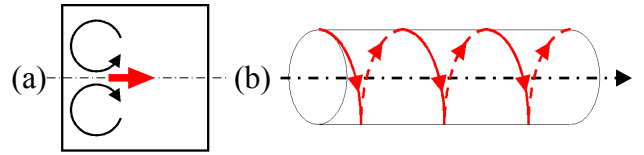
Skecth.2. (a) Induced velocity caused by a pair of vortices in the duct section; *Biot-Savart law*, (b) *Helicity* structure similar to electronic coil systems. Cylinder form; iso-surface of *helicity* corresponds to coil cylinder and red line; stream-line corresponds to coil helix.
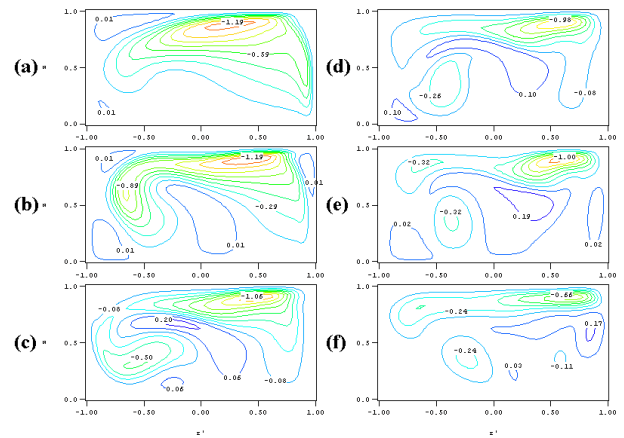

Fig.8. *Helicity* variation along azimuthal direction θ for case.   at θ = (a) 30, (b) 45, (c) 60, (d) 75, (e) 90 and (f) 120-degrees half-top sections.
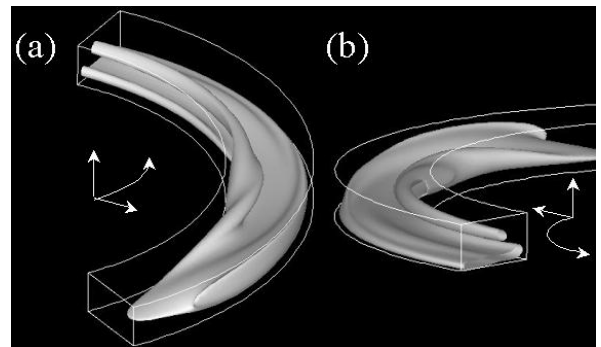

Fig.9 Iso-surface of positive *helicity*; +0.1 in half-bottom area of case.   . Views from (a) the inlet and (b) the outlet.
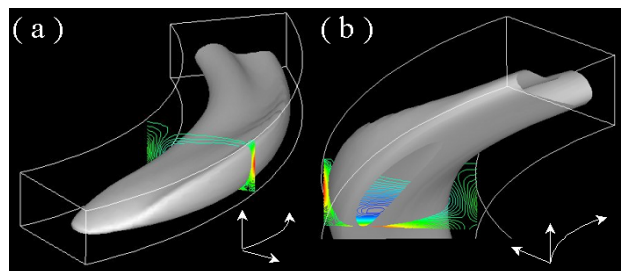

Fig.10 Iso-surface of positive *helicity*; +0.05 with stream-wise vorticity ω_θ (contours) at θ =29-degrees section in half-bottom area for preliminarily tests; (a) inlet view for front section and (b) elevation view from bottom wall and outlet section.

3.3 Inflection point and compressible effect for a curved duct flow of case.

Fig.11 shows the distributions of stream-wise velocity and temperature at the different downstream sections for case. . Fig.11(d) at the outlet section shows that the high temperature region as well as the stream-wise velocity close to the concave wall is affected by the vortices generating on the outside-wall shown in Fig.6(d). Here, the distribution of the stream-wise velocity u_θ in Fig.11(d) is similar to the incompressible case [7] with $D_n = 453.0$ that the flow has a *6-cell state*. Therefore, the outflow boundary conditions with $\sigma = 0.25$ is found to give an appropriate solution for this flow. The temperature inside the vortex is slightly low. In Fig.11(c) when a *4-cell* state develops, higher temperature regions around at $r'=0.3$ and $z=0.6$ are transported into the inside part of the duct section by the stronger counter-rotating vortices generating around the location of $r'=-0.4$ and $z=0.4$ as shown in Fig.6(c). But, at the outlet section, this phenomenon is damped and more stable a *2-cell* state develops rather than a *4-cell* state.

The flow is unstable when the mean velocity has an inflection point. Fig.12 and Fig.14 indicate the contours of the second derivatives
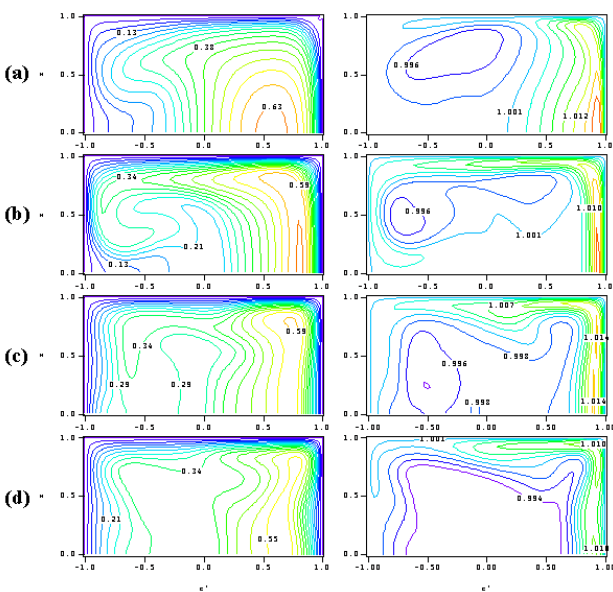

Fig.11. Contours of stream-wise velocity u_θ (left) and temperature (right) for case. at (a) 30, (b) 60, (c) 90 and (d) 120-degrees sections.

of the stream-wise velocity u_θ in each direction at the 30-degrees and the 90-degrees sections, respectively. Note that the intervals of the contour and the threshold value for each direction are the same in the section distributions. Near the top/bottom and the concave walls, the gradients of u_θ in the r-direction are steeper than that in z-direction at the 30-degrees section. On the contrary, further downstream, the gradients of u_θ in the z-direction are steeper than that in the r-direction at the 90-degrees section.

Fig.13 indicates the section distributions of u_θ in the r-direction at the 30-degrees section. In Fig.13(a), the section distributions of u_θ at the same stations correspond to the locations expressed dotted lines with the same colors in Fig.12. Fig.13(b) shows the section distributions of the inflection points at the same stations in Fig.13(a). Although the inflection points near the concave wall don't appear clearly excepted at the section of $z=0.88$ in Fig.13(a), they are obtained by the calculation shown in Fig.13(b). Similar to Fig.13, Fig.15 indicates the section distributions of u_θ in the z-direction at the 90-degrees section. In Fig.15(a), the section distributions of u_θ at the same stations correspond to the locations expressed dotted lines with the same colors in Fig.14. Fig.15(b) shows the section distributions of the inflection points at the same stations in Fig.15(a). Although the inflection points near the top wall don't appear clearly in Fig.15(a), they are also obtained by the calculation shown in Fig.15(b). Obviously in Fig.14, the inflection points of the r-direction along with concave wall disappear at the 90-degrees section while the inflection points of the z-direction appear near the top wall. Compressible effects are investigated. Vorticity equations for compressible flows, sometimes called as *Friedman equation,* are

$$\frac{\partial \vec{\omega}}{\partial t} + (\vec{u} \bullet \nabla) \, \vec{\omega} =$$

$$(\vec{\omega} \bullet \nabla) \, \vec{u} - (\nabla \bullet \vec{u}) \, \vec{\omega} - \nabla\left(\frac{1}{\rho}\right) \times \nabla p \ . \ (14)$$

Fig.16 shows that the gradients of pressure and density are not necessarily parallel, for example,

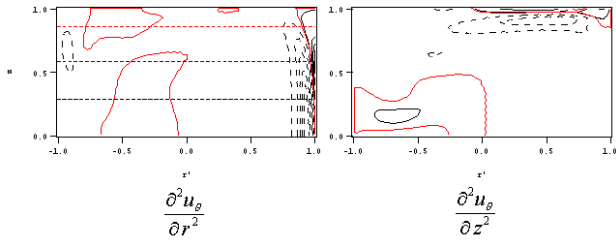$$\frac{\partial^2 u_\theta}{\partial r^2} \qquad \frac{\partial^2 u_\theta}{\partial z^2}$$

Fig.12. Distributions of the inflection points at the 30-degrees section in case.　. Black lines: contours of d$^2u_\theta$/dr^2 (left) and d$^2u_\theta$/dz^2 (right) from –57.3 to 37.3 at intervals of 10.0 (continuous: positive and dotted: negative) and red lines: 0-gradient contours.
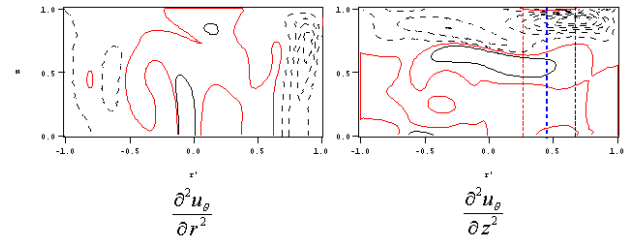

$$\frac{\partial^2 u_\theta}{\partial r^2} \qquad \frac{\partial^2 u_\theta}{\partial z^2}$$

Fig.14. Distributions of the inflection points at the 90-degrees section in case.　. Black lines: contours of d$^2u_\theta$/dr^2 (left) and d$^2u_\theta$/dz^2 (right) from –53 to 17 at intervals of 8 (continuous: positive and dotted: negative) and red lines: 0-gradient contours.
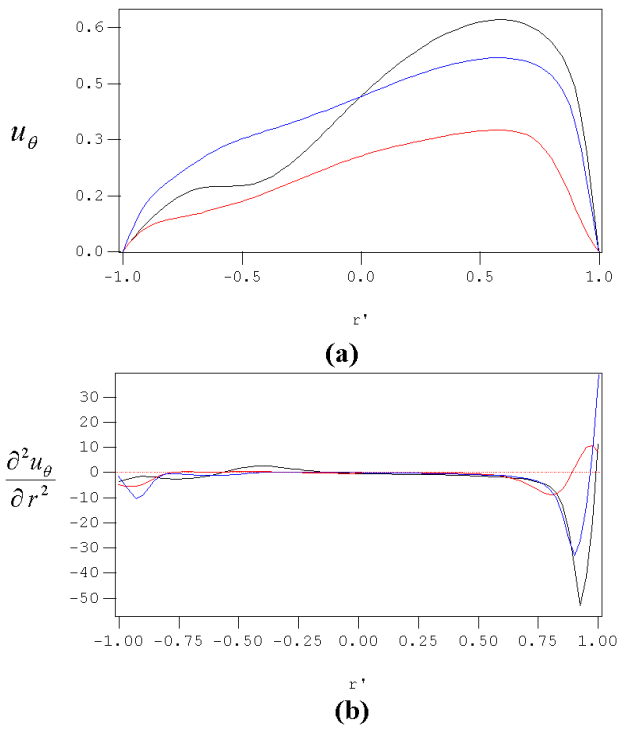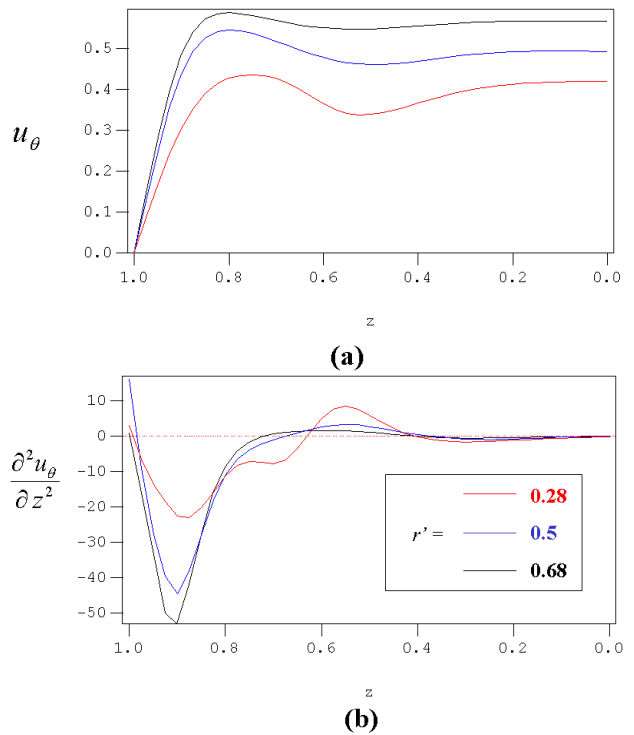

(a)

(b)

Fig.13. (a) Distributions of stream-wise velocity u_θ normalized by sonic speed on the wall at the 30-degrees section in case.　. Black line: z =0.27, blue line: z =0.6 and red line: z =0.88. (b) Section distributions of the second derivative in r-direction of u_θ at the several z-stations in Fig.12.
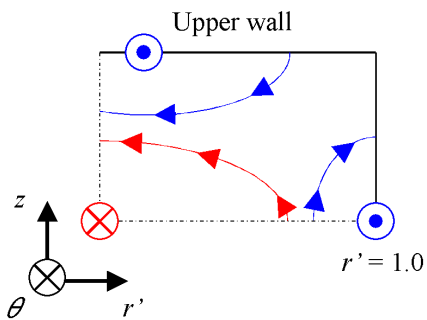

(a)

(b)

Fig.15. (a) Distributions of stream-wise velocity u_θ normalized by sonic speed on the wall at the 90-degrees section in case.　. Black line: r' =0.68, blue line: r'=0.5 and red line: r'=0.28. (b) Section distributions of the second derivative in z-direction of u_θ at the several r'-stations in Fig.14.
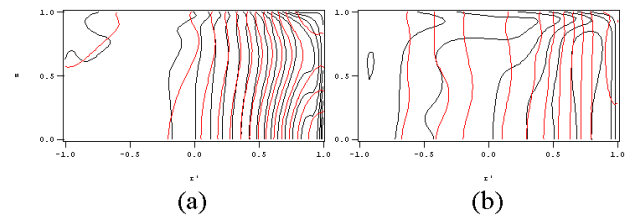

(a)　　　　(b)

fig.16. Contours of density and pressure at (a) the 30 and (b) the 90-degrees sections for case.　: black and red lines indicate density and pressure, respectively.

Skecth.3. Distributions of vorticities 　　 around the corner (see fig.6).

see the results at (a) the 30-degrees and (b) the 90-degrees sections. Therefore, Fig.17 indicates the source of the vorticity ω_θ the stream-wise component of Eq.(14), which appears on the bottom wall. It is, however, very small. Then, by supplying ω_θ on the walls, the *helicity* by these voticities, as illustrated in sketch.3, may be maintained with its strength downstream slightly longer than the incompressible cases.

The generalized inflection points of the *i*-direction are defined as

$$\frac{\partial}{\partial x_i}\left(\rho\,\frac{\partial u_\theta}{\partial x_i}\right)=0 \cdot \qquad (15)$$

Decomposing Eq.(15) into

$$\frac{\partial \rho}{\partial x_i}\frac{\partial u_\theta}{\partial x_i}+\rho\,\frac{\partial^2 u_\theta}{\partial x_i^2}=0, \qquad (16)$$

the first term of Eq.(16) shows compressible flow effects due to density distribution. Fig.18 shows the contours of density gradients for each direction. The intervals of the contour and the threshold value for each direction are the same. In addition, red and black lines indicate the generalized inflection points and ordinary inflection points, respectively. Steep gradient of density for each direction appears around the same place of the inflection points. Fig.19 shows the generalized inflection points compared with ordinary inflection points for each direction at the sections of the 30-degrees (a) and the 90-degrees (b), respectively. The compressible effects, appear in Fig.18, on appearance of the generalized inflection point are small in this flow.

4 Conclusions

DNS code with *NSCBC* giving good agreements with an analytical solution for very low *Re* flows is employed for higher D_n flow calculations. For duct flows with very low curvature ratios, stream-wise velocity and secondary flow are resulted in much similar to incompressible cases. In this study, temperature profile transported by *Dean* vortices is observed when a *4-cell* state appears. To understand the essential stream-wise structure, *helicity* structures involving three-dimensional vortices effect are researched. Due to the induced veloci-
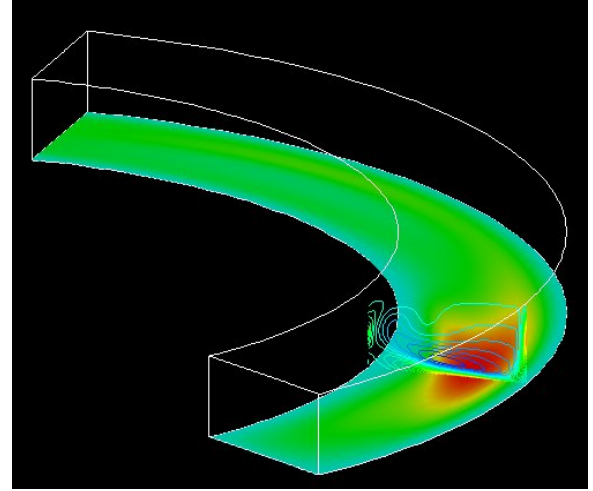

Fig.17. Source distribution of   (red region) on the bottom wall with contours of   at the 30-degrees section for case.   . Front; inlet view.
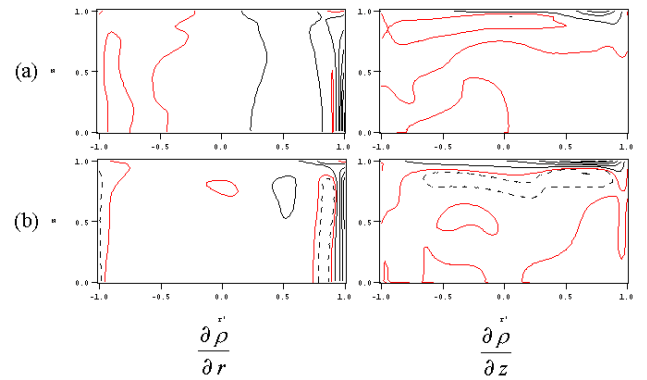

Fig.18. Contours of density gradients at (a) θ=30 and (b) 90-degrees sections in case.   . Black lines: contours from (a) -0.1 to 1.2 at intervals of 0.2 and (b) -0.2 to 0.8 at intervals of 0.15 (solid: positive and dotted: negative) and red lines indicate 0-gradient contours.
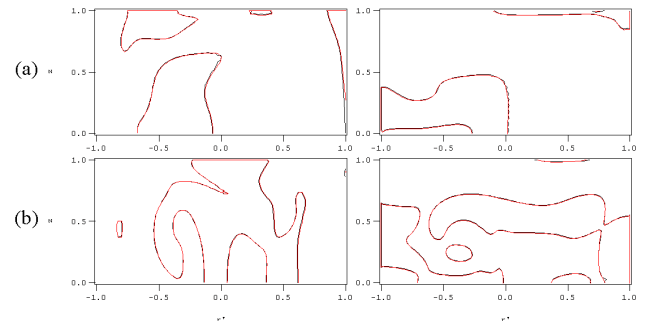

Fig.19 Comparison of contours for the inflection points. Black; the inflection points of $d^2 u_\theta$ /dr^2 (left) and $d^2 u_\theta$ /dz^2 (right) shown in Fig.12 and Fig.14 and red; the generalized inflection points of d/dr (ρ du_θ/dr) (left) and d/dz (ρ du_θ/dz) (left) at (a) θ=30 and (b) 90-degrees sections.

ty by the strong interaction between a pair of vortices, H^2-structures are observed around about the 60-degrees section where the secondary flow develops into a *4-cell* state from a *2-cell* state. The section distributions of *helicity* indicate several vorticity structures with small/large amplitudes. Although the inflow conditions researched in this study is very simple, complex structures such as H^2-structures are observed. This may be much important for problems such as a gap flow between gas turbine blades. Actually, it is well known for such a flow that corner vortices correspond to H^2-structures interact strongly with horseshoe vortices in steady state. From this study, the inflection points near the walls may appear on the concave wall around the 30-degrees section. At further downstream, the inflection points may appear on the top/bottom walls. Although compressible effects are observed in the generation of vorticity, these influences for the location of the generalized inflection points are small. Due to the generations of vorticity on the walls, appearance of the inflection points with a maximum shear close to the walls will lead to transition to turbulence in the curved duct flows at high D_n numbers.

References

[1] T. J. Poinsot and S. K. Lele, *Boundary condition for direct simulations of compressible viscous flows*, *J. Comp. Phys.* Vol. 101, pp 104-129, 1992.

[2] S. K. Lele, *Compact finite difference scheme with spectral-like resolution*, *J. Comp. Phys.* Vol. 103, pp 16-42, 1992.

[3] W. Y. Soh, *Developing fluid flow in a curved duct of square cross-section and its fully developed dual solutions*, *J. Fluid Mech.* Vol. 188, pp 337-361, 1988.

[4] P. Hille, R. Vehrenkamp and E. O. Schulz-Dubois, *The development and structure of primary and secondary flow in a curved square duct*, *J. Fluid Mech.* Vol. 151, pp 219-241, 1985.

[5] P. A. J. Mees, K. Nandakumar and J. H. Masliyah, *Secondary instability of flow in a curved duct of square cross-section*, *J. Fluid Mech.* Vol. 3323, pp 387-409, 1996.

[6] B. Bara, K. Nandakumar and J. H. Masliyah, *An experiment study of the Dean problem: flow development towards two-dimentional multiple solutions*, *J. Fluid Mech.* Vol. 244, pp 339-376, 1992.

[7] P. A. J. Mees, K. Nandakumar and J. H. Masliyah, *Instability and transitions of flow in a curved duct: the development of two pairs of Dean vortices*, *J. Fluid Mech.* Vol. 314, pp 227-246, 1996.

[8] D. Watanabe and H. Maekawa, *Instabilityof streamwise vortices in a curved duct*, *CFD symposium 14th*, Tokyo, B03-2, 2000.

[9] K. Ozaki and H. Maekawa, *CFD symposium 16th*, Tokyo, 2002.

[10] K. Ozaki and H. Maekawa, *Curvature effect in the curved duct for the compressible viscous flow with heat transfer*, *FEDSM'03 4th ASME_JSME Joint Fluid Engineering Conference*, Hawaii, FEDSM2003-45634, 2003.